Microporous and Mesoporous Materials 310 (2021) 110589

Contents lists available at ScienceDirect

Microporous and Mesoporous Materials

journal homepage: http://www.elsevier.com/locate/micromeso

Enhanced anticancer performances of doxorubicin loaded macro-mesoporous silica nanoparticles with host-metal-guest structure

Ruoshi Zhang [a], Xin Wang [b], Na Fan [b], Jing Li [a,*]

[a] School of Pharmacy, Shenyang Medical College, Shenyang, China
[b] Wuya College of Innovation, Shenyang Pharmaceutical University, Shenyang, China

ARTICLE INFO

Keywords:
Magnetic modification
Mesoporous silica nanoparticles
Doxorubicin hydrochloride

ABSTRACT

Fe(III) loaded porous silica nanoparticles have great value for establishing anticancer drug delivery system. In this study, host-metal-guest carrier named as MM–SN–NH_2-Fe was obtained by grafting aminopropyl and Fe(III) onto macro-mesoporous silica nanoparticles (MM-SN). Doxorubicin hydrochloride (DOX) has been chosen as a model anticancer drug and the NH_2–Fe-DOX coordination bond structure has been constructed on the pore surface using the iron necessary for the organism. The release performance of DOX loaded MM–SN–NH_2-Fe showed higher pH response release by cleavage of the Fe-DOX bond or the NH_2–Fe coordination bond. Cytotoxicity assay indicated that DOX loaded MM–SN–NH_2-Fe presented stronger anti-cancer activity against MCF-7 and MCF-7/ADR cells compared to that of free DOX and DOX loaded MM-SN. In vivo, DOX based nanoparticles significantly prolonged systemic circulation and DOX loaded MM–SN–NH_2-Fe presented the best antitumor effect. As expected, we developed a novel carrier with pH-triggered release and high anti-cancer activity for DOX delivery system, which has great value in anticancer treatment.

1. Introduction

Breast cancer is one of the most serious diseases that harms women's health all over the world [1]. Chemotherapy, as an effective treatment method, plays an important role in the treatment of breast cancer. However, its application failed due to the severe side effects [2]. In chemotherapy, multidrug resistance (MDR) is one of the major challenges known to all the researchers. One of the effective strategies to reverse MDR is to use nanoparticle-mediated drug delivery so that high drug concentration can be achieved. In this study, we applied an inorganic delivery system based on loaded doxorubicin (DOX) mesoporous silica nanoparticles to achieve superior drug delivery effects, including the reduction of MDR of MCF-7/ADR (a DOX-resistant and *P*-glycoprotein over-expression cancer cell line) [3]. DOX, a potent water-soluble anti-tumor drug, was applied as model drug in this study. It is used as the first-line approach for treating breast, bile ducts, prostate, uterus, ovary and oesophagus, stomach liver tumors, as well as childhood solid tumors, osteosarcomas and soft tissue sarcomas [4–7]. The chemical structure of DOX was displayed in Fig. 1A. It is reported that DOX molecule can form strong hydrogen bonding forces with other hydroxyl radical or amino groups, which lays foundation for the theory of pH-triggered DOX release in the medium [8]. It has been reported that DOX has a high affinity for inorganic iron, Fe(III), and has potential to form DOX-Fe(III) complexes whose chemical structure was shown in Fig. 1B [9]. Furthermore, DOX-Fe(III) complex causes the mutagenicity through oxidative DNA damage and Fe(III) is required. The mutagenicity of DOX-Fe(III) complex cause oxidative DNA damage due to free radicals formed from the interaction of DOX with Fe(III). Therefore, the DOX dose can be reduced [9,10], which has been well reported [11–14].

In recent years, porous silica nanoparticles have been extensively studied by researchers expert in the field of biomedical applications owing to their superior characteristics including:(1) good biocompatibility and biodegradablity; (2) adjusted pore size; (3) high drug loading capacity due to large surface area and pore volume; (4) facile and abundant surface modifications with extra advantages in delivering guest molecules [15–25]. Compared to naked porous silica nanoparticles, the porous silica nanoparticles decorated with functional groups can enhance drug loading capacity and influence the drug release behavior. It has reported that the surface modification of porous silica nanoparticles has an effect on their adsorption and release properties to some extent [8,24,26]. Porous silica nanoparticles linked with amino group can be performed via two routes according to the literature [21],

* Corresponding author. , No. 146 Huanghe North Street, Shenyang, Liaoning Province, China.
E-mail address: dddefghijklmn@163.com (J. Li).

https://doi.org/10.1016/j.micromeso.2020.110589
Received 14 June 2020; Received in revised form 20 August 2020; Accepted 24 August 2020
Available online 11 September 2020
1387-1811/

including co-condensation method and post-synthesis method. Currently, stimuli-response drug delivery systems have been paid increasing attention in recent years owing to "intellectual" functions in biomedical science [27–29]. After administration, nanocarriers leak out and accumulate at the tumor tissues via enhanced permeability and retention effect or active targeting. Then, the drug delivery systems can be triggered from inner or outer environment and delivered drugs to the intended location [30]. Porous silica nanoparticles have been considered as potential carries owing to their distinctive characteristic [31–33], especially for acid-responsive drug delivery systems since pH gradients present in different tissues and subcellular compartment [34,35].

As known to all, porous silica nanoparticles consist of microporous silica nanoparticles, mesoporous silica nanoparticles and macroporous silica nanoparticles, and the latter two are mostly used as drug carriers. Mesoporous silica with pore diameter of 2–50 nm can be prepared by via micelles or liquid crystals based on cooperative templating mechanism or liquid crystals templating method [36–38]. Macroporous structures with pore diameter higher than 50 nm have also been synthesized by different templates, including latex spheres, solid lipid nanoparticles and emulsions [39]. The application of macroporous silica nanoparticles can provide advantages for loading guest molecules [40,41]. It had reported that combination of mesopores and macropores can be realized by using tetradecyltrimethylammonium bromide (TTAB) and Pluronic P123 as templates [39]. Different from these previous reported works, the present paper tried to explore the formation of macro-mesoporous silica nanoparticles (MM-SN) synthesized using one template under simple systemic condition.

Herein, we have developed a pH-triggered drug delivery system by grafting amino groups onto MM-SN and these amino groups adsorb Fe (III), then Fe(III) attracts with DOX, resulting in 'host–metal–guest' structure, where 'host', 'metal' and 'guest' represent amino groups on the silica nanopore surface, iron ions, and DOX molecules, respectively [21]. The novelty of this paper can be concluded as: (1) the preparation of MM-SN is easy to control by using only one template under simple systemic condition; (2) MM-SN is used to graft amino groups because it can load more amino groups than mesoporous silica nanoparticles [8]; (3) the advantages of MM–SN–NH_2-Fe-DOX are not only for its pH-triggered drug delivery owing to amino groups but also for DOX-Fe (III) complex with superior DNA damage effect. The deliver performances of this drug loading system were mainly focused, including pH stimuli release, cytotoxicity and MDR reversion.

2. Materials and methods

2.1. Materials

Tetraethylorthosilicate (≥99%, TEOS) and absolute ethyl alcohol were purchased from Tianjin Bodi Chemical Co. LTD. Hydrochloric acid (36%–38%), sodium hydroxide (≥96%), dipotassium phosphate (≥99%), NH_4F and octane were bought from Xilong Chemical Co. LTD. Pluronic P123 was purchased from Sigma Aldrich. Deionized water was obtained using a Milli-Q water purification system.

2.2. Synthesis of MM-SN

MM-SN was prepared with P123 as template and TEOS as silica source. Briefly, 2.4 g P123 was dissolved in HCl solution (1.3 M) and stirred at 25 °C. NH_4F was added into the system. Afterwards, octane (11.08 g) and TEOS (4.03 g) were added under stirring (P123: HCl: NH_4F:H_2O: octane: TEOS molar ratios = 1 : 261: 1.8 : 11,278: 235 : 50). The above mixture was stirred and then transferred into an autoclave for further hydrothermal treatment. The products were collected by filtration, washed with deionized water for three times and dried at 40 °C vacuum drying oven for 24 h. Finally, the template was removed by calcination at 550 °C for 6 h.

2.3. Preparation of MM–SN–NH_2-Fe

MM-SN was mixed with 20 mL APTES in 100 mL toluene. The mixture was stirred for 24 h under the protection of nitrogen. The obtained samples were centrifuged and washed with toluene, methanol and finally water. Afterwards, the white solid product was dried. Stock solution of ferric ions was prepared by dissolving $Fe(NO_3)_3$ in deionized water. In a typical loading process, 0.25 g of the above product was dispersed in 20 mL of the stock solution, and the mixture was stirred mildly at ambient temperature for 2 h. Finally, the products were collected by centrifugation, then washed with ethanol until the supernatants were colorless and dried overnight [21].

2.4. Characterization

2.4.1. TEM

The porous structure of MM-SN was characterized using Tecnai G2 20 instrument (FEI, the United States). Sample was dispersed in ethanol solution and then displayed onto porous carbon films before being scanned.

2.4.2. Nitrogen adsorption/desorption measurement

The pore volume and surface area of MM-SN were conducted by studying the nitrogen adsorption and desorption using a SA3100 surface area and pore size analyzer (Beckman Coulter, USA). Before measurement, samples were dried at 40 °C vacuum drying oven for 24 h.

2.4.3. FTIR

FTIR (Spectrum 1000, PerkinElmer, USA) spectra of samples (MM-SN and MM–SN–NH_2) were recorded from 400 to 4000 cm^{-1} in transmittance mode with a resolution of 1 cm^{-1}. Samples were prepared by gently and respectively grounding samples with KBr.

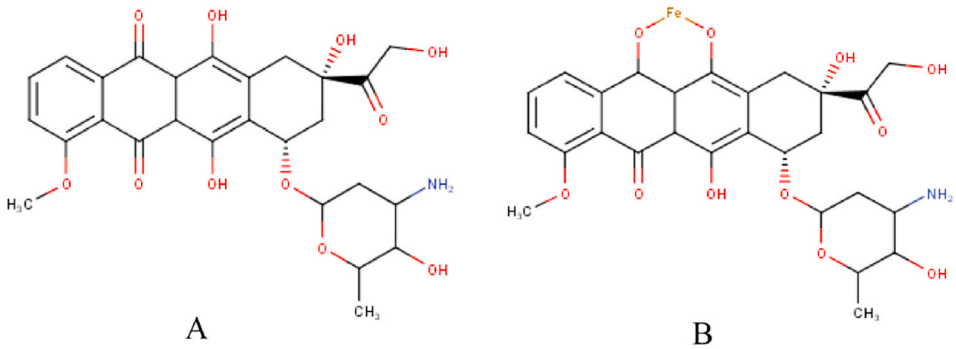

Fig. 1. The chemical structures of (A) DOX molecules and (B) DOX-Fe (III).

2.4.4. Zeta potential measurement

Zetasizer Nano ZS (Malvern Instruments, Malvern, UK) was applied to measure the zeta potential of samples that dispersed in pH 7.4 PBS solution. Each sample was conducted for three times.

2.4.5. XPS analysis

XPS analysis was conducted using Thermo K-alpha spectrometer with a hemispherical analyzer. Working conditions included 400 mm diameter microspot, monochromated radiation of 72 W under a residual pressure of 10^{-9}.

2.5. Hemolysis assay

Hemolysis was one of the most important concerns when administrating MM-SN through vein injection route. The rat red blood cells were obtained by centrifugation and removed the serum from the blood and then washed with sterile normal saline solution until the supernatant was clear. The red blood cells were diluted 50 times of their volume with physiological saline solution. Subsequently, the diluted rat red blood cells suspension was mixed with saline solution as a negative control. In the meanwhile, the diluted rat red blood cells suspension was dispersed into physiological saline solution at the different concentrations. Positive control was made by mixing the diluted rat red blood cells suspension with distilled water. All mixtures were shaken well at room temperature and centrifuged. The absorbances of supernatant at 541 nm were recorded by the ultraviolet spectroscopy (UV-1750, Shimadzu, Japan) and finally hemolysis ratio was calculated.

2.6. Drug loading and in vitro release

Briefly, a total of 100 mg carrier was mixed with 1 mL DOX anhydrous ethanol solution (50 mg/mL). After stirring for 24 h under dark conditions, DOX loaded MM-SN or DOX loaded MM–SN–NH_2-Fe was centrifuged and washed five times using anhydrous ethanol. Finally, these samples were dried under vacuum oven at room temperature and stored at dark conditions. Drug loading capacity was measured by taking an accurately weighed quantity of DOX loaded carrier, then extracting the loaded DOX completely using anhydrous ethanol under ultrasound, and finally measuring DOX content with ultraviolet spectroscopy (UV-1750, Shimadzu, Japan) at the wavelength of 499 nm. Drug loading capacity was calculated according to the following equation.

$$\text{Drug loading capacity } (\%) = (W_{\text{drug in nanoparticles}} / W_{\text{nanoparticles}}) \times 100$$

To confirm drug was loaded into the pores of carrier, nitrogen adsorption and desorption measurement of DOX loaded MM-SN and DOX loaded MM–SN–NH_2-Fe were conducted (see supporting information Table 1). *In vitro* release study was carried out as follows. The dialysis bags containing samples were put into dissolution medium (PBS 7.4 and PBS 5.0) that kept warmed at 37 °C with shaking speed of 100 rpm. At predetermined time intervals, 3 mL of the resultant release medium was withdrawn in a centrifuge tube for analysis and then 3 mL fresh corresponding dissolution medium was promptly added to maintain the original volume. The DOX concentration was measured using UV spectroscopy (UV-1750, Shimadzu, Japan).

2.7. Cell culture

Human drug-sensitive breast cancer cells (MCF-7) were cultured in dulbecco's modified eagle medium supplemented with 10% fetal bovine serum (FBS), penicillin (100 units/mL) and streptomycin (100 μg/mL), under a humidified atmosphere containing 5% CO_2. The cells were subcultured until 85% confluence by using trypsin-EDTA to digest for 90 s and the culture medium was replaced once every two days. Human multidrug resistant breast cancer cells (MCF-7/ADR) were grown at 37 °C in a humidified atmosphere containing 5% CO_2 in Gibico 1640 medium with 10% FBS and 1% antibiotics (100 Unit mL^{-1} penicillin G sodium and 100 μg/mL streptomycin sulfate).

2.8. Cell viability studies

The cell viability of MM-SN, MM–SN–NH_2-Fe, DOX solutions, DOX loaded MM-SN and DOX loaded MM–SN–NH_2-Fe were evaluated by MTT assays. Briefly, MCF-7 cells were seeded at a density of 5000/200μL/well into 96-well plates in 200 μL of culture medium with 10% FBS. Similarly, MCF-7/ADR cells were seeded at 96-well plates with a density of 6000/well supplemented with 200 μL of culture medium containing 10% FBS. The cells were grown for 12 h and then were exposed to various silica carriers with concentrations ranging from 2 to 50,000 ng/mL. Thereafter, the culture medium containing drugs was replaced by 100 μL fresh medium without FBS, and then 20 μL sterile MTT solution (5 mg/mL in PBS) was added to each well, and incubated for additional 4 h at 37 °C, which allowed live cells reduce MTT into dark-blue formazan. Then, the media was completely removed, and 150 mL DMSO was added to each well to dissolve MTT formazan and the plate was shaken mildly at room temperature for 10 min on a shaking platform under dark condition. The absorbance was detected at a wavelength of 570 nm by a BioRadicroplate reader (Model 500, USA). The Cell viability rate and IC_{50} value were calculated.

2.9. Pharmacokinetics

Animals experiments were performed according to the Guide for Care and Use of Laboratory Animals approved by the Institutional Animal Ethical Care Committee of Shenyang Pharmaceutical University.

Nine fasted Sprague-Dawley rats (200–220 g) were randomly divided into three groups to carry out the pharmacokinetic study. DOX solution, DOX loaded MM-SN and DOX loaded MM–SN–NH_2-Fe at a single dose of 5 mg/kg with equivalent DOX were administrated by tail vein injection. At predetermined time intervals, approximately 0.5 mL blood samples were transfer into a centrifuge tube coated with heparin sodium, then the centrifuge tube was centrifuged at 13,000 rpm for 10 min to obtain serum. After that, the plasma samples were stored at −20 °C until analysis. The HPLC-MS/MS apparatus was used to determine the concentration of free DOX solution and two preparations in rat plasma. XB C18 column (50 × 2.1 mm, 2.6 μm, Phenomenex) was employed for chromatographic separation. The mobile phase was consisted of methanol (A) and water containing formic acid (B) for chromate graphic separation at a flow rate of 0.5 mL/min. To determine DOX, elution of 55% A and 45% B was performed.

2.10. Pharmacodynamics

4 T1 cells were cultured to logarithmic phase, and then washed using PBS for 3 times and diluted the cells to the density of 1 x 10^6 cells mL^{-1}. Healthy Balb/C mice were given intraperitoneal injection of 0.2 mL cells. After the abdominal cavity of the mice was filled with ascites, the mice were killed, and the animal skin was sterilized with iodine volts. The ascites were transferred to a sterile ultra-clean table to extract the ascites, and sterile PBS was added to dilute the cell suspension to a density of 1 × 10^6 cells ml^{-1}. The suspension of 0.2 mL 4T1 cells was inoculated under the subcutaneous surface of the right axilla of mice to establish the axillary inoculation model of 4T1 tumor strain of breast cancer. Follow-up experiments were performed when the tumor volume reached about 100–200 mm^3. Tumor-bearing mice were randomly divided into 4 groups with 10 mice in each group and divided into normal saline group (model group), DOX solution group, DOX loaded MM-SN group and DOX loaded MM–SN–NH_2-Fe group. The drug was given every 1 day for 3 times at a dose of 10 mg kg^{-1}. After administration, the survival state of the mice was observed every 1 day, the body weight was measured, the average body weight of each group was calculated, and the systemic toxicity of each preparation was

investigated. The tumor volume was measured with vernier caliper to investigate the anti-tumor effect of each preparation. Mice were sacrificed on the 11th day after drug administration, the tumor was removed, the surface was washed with normal saline, the filter paper was sucked dry, and the tumor inhibition rate was calculated.

3. Results

3.1. Characterization

Obviously, as seen in Fig. 2A, the obtained particles were relatively uniform and showed layer-by-layer appearance with approximately 60–100 nm in width and 100–200 nm in length. According to the IUPAC classification, the nitrogen adsorption/desorption isotherm of MM-SN exhibited type IV isotherms with two distinct adsorption peaks at the relative pressure of 0.45–0.8 and 0.8–0.99, respectively as shown in Fig. 2B. The first step was corresponded to nitrogen capillary condensation in the common mesopores of MM-SN, resulting in a relatively narrow peak in the pore size distribution curve. The second adsorption step, where relative pressure p/p_0 equal to 0.8–0.99, causing a broad pore size distribution, corresponding to the secondary enlarged nanopores, which were macropore as observed in the TEM images. The displayed two hysteresis loops were conclusive evidence for demonstrating the multimodal nanoporous structure of MM-SN [42]. According to pore diameter distribution curve, the first phase of pore diameter located in the range of 2–50 nm and the second phase covered pore diameter from 50 nm to 100 nm, further confirmed the macro-mesoporous structure of MM-SN and was in agreement with adsorption/desorption isotherm result. The BET surface area of MM-SN was found to be 745.18 m^2/g and the total pore volume was 2.04 cm^3/g. MM-SN with such significant large pore volume can be of great interest among the family of nanoporous silica nanoparticles.

The FTIR spectra of the two samples, MM-SN and MM–SN–NH_2, were illustrated in Fig. 2C. For MM-SN, the adsorption peak observed at 3424.8 cm^{-1} corresponded to antisymmetric stretching vibration of Si–OH and the band assigned to Si–*O*–Si bending vibration shown in 464.1 cm^{-1}. In addition, the band displayed in 1082.9 cm^{-1} was consistent with Si–*O*–Si antisymmetric stretching vibration [42,43]. We can infer that MM-SN was synthesized successfully according to the above data. In the FTIR image of MM–SN–NH_2, the band evidenced at 1631.5 cm^{-1} was attributed to deformation vibration of amino group, and the band resulted from CH_2 stretching were shown at 2928.3 cm^{-1} due to the methyl groups introduced during grafting process. Moreover, the NH_2 stretching mode can be observed at 3424.9 cm^{-1}. The presence of these peaks can confirm successful grafting amino groups.

The analysis result of zeta potential values was shown in Fig. 2D. The zeta potential value of MM-SN was −5.64 mv owing to the silanol groups existing on the surface. After decoration, the zeta potential of MM–SN–NH_2 increased by 14 mv approximately to 8.28 mv due to the introduction of positive electricity of the aminopropyl group. In this case, the number of surface hydroxyl groups that reacting with the APTES to form Si–*O*–Si bonds was reduced. This reduction in the hydroxyl groups suggested an anchoring mechanism involving a reaction between the silanol groups and APTES [44]. It can be decided from above results that MM-SN were successfully functionalized by aminopropyl groups. Moreover, after Fe(III) was loaded into the nanopores, the potential value (up to 28.8 mv) became higher than unloaded particles. Based on the zeta potential analysis, we can preliminarily judge that Fe(III) was incorporated into the nanopores of MM–SN–NH_2.

The XPS analysis results were shown in Fig. 3. For MM-SN, XPS analysis evidenced the presence of carbon (8.98 at%), oxygen (57.69 at %) and silicon (33.33 at%). As a comparison, XPS analysis of

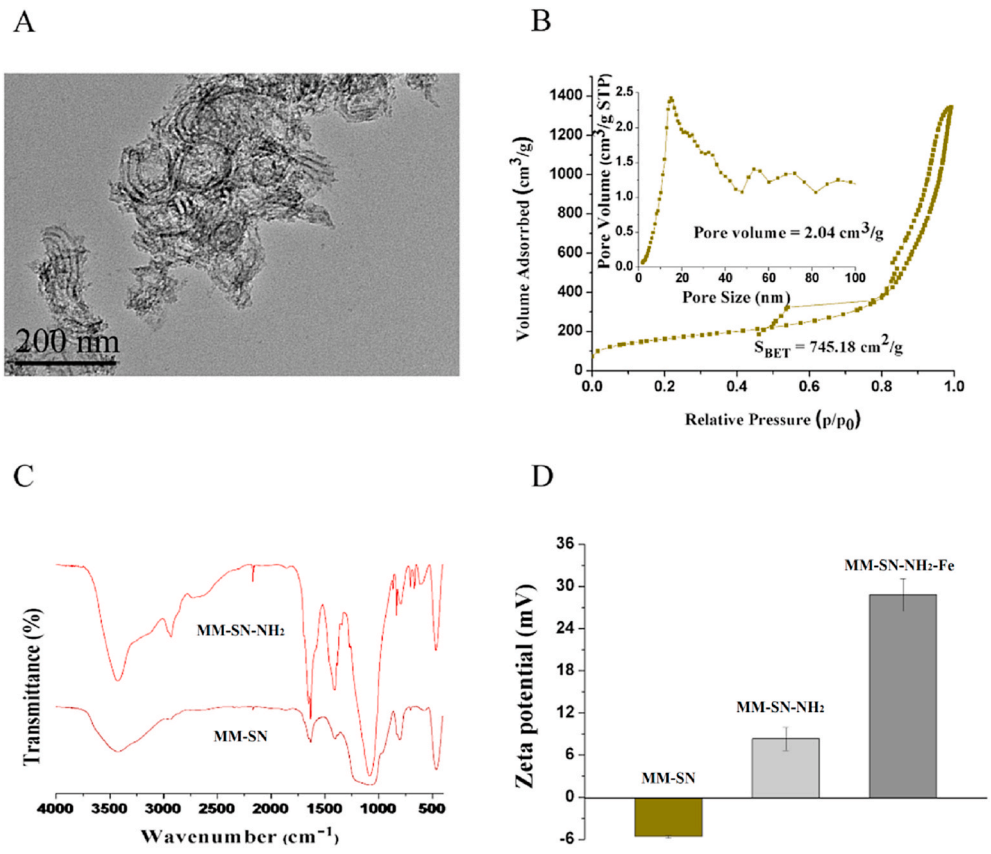

Fig. 2. Characterization of the two samples. (A) TEM image,(B) nitrogen adsorption/desorption isotherm of MM-SN, (C)FTIR spectra of MM-SN (bottom) and MM–SN–NH_2 (top), and (D) zeta potential analysis result.

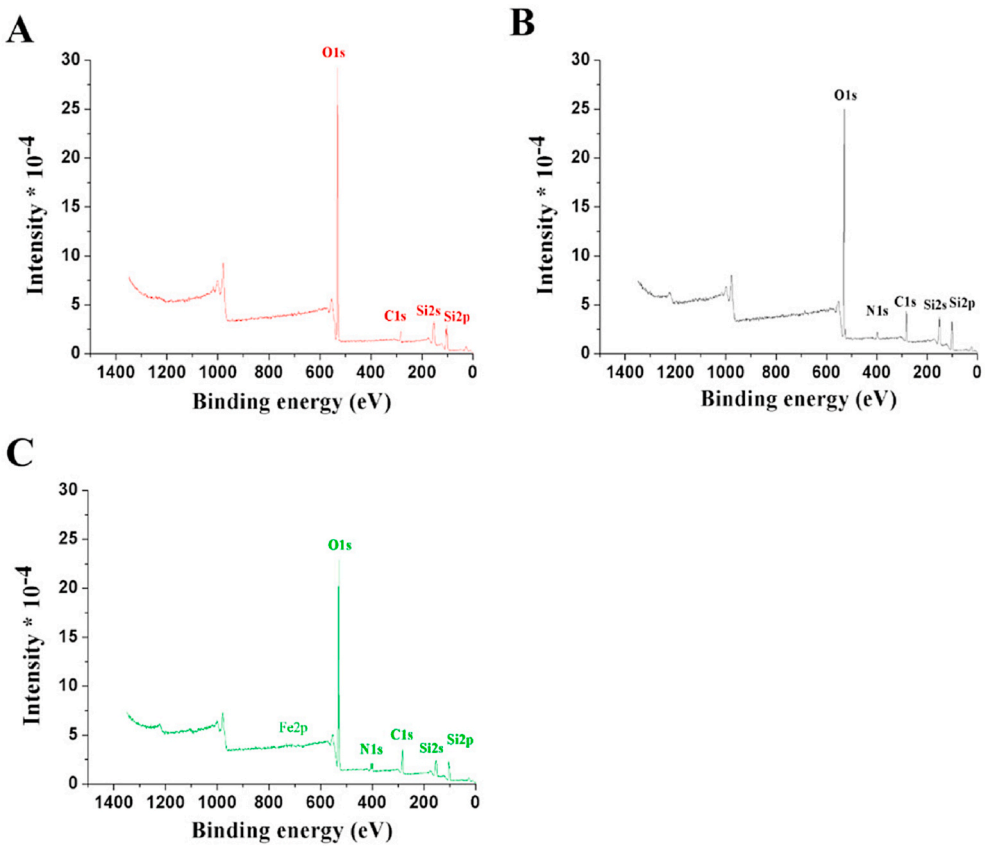

Fig. 3. XPS analysis results of (A)MM-SN, (B) MM–SN–NH_2 and (C) MM–SN–NH_2-Fe.

MM–SN–NH_2 elucidated the existence of carbon (21.51 at%), oxygen (46.43 at%), silicon (28.51 at%) and nitrogen (3.55 at%). When comparing MM–SN–NH_2 to MM-SN, we can learn that the carbon contamination was higher and the content of silicon and oxygen were lower, which was the result of introducing aminopropyl groups. Moreover, it displayed the nitrogen element in the MM–SN–NH_2. The XPS analysis further confirmed that the MM-SN was functionalized with aminopropyl groups successfully. As for MM–SN–NH_2-Fe, the contents of carbon, oxygen, silicon, nitrogen and iron demonstrated in XPS analysis were 23.48 at%, 45.64 at%,24.63 at%, 5.74 at% and 0.52 at%, respectively.

3.2. Biocompatibility of MM-SN and MM–SN–NH_2-Fe

Hemolysis assay and cell viability studies were conducted to certify the biocompatibility of MM–SN–NH_2-Fe for practical biomedical applications [45]. According to Fig. 4A and Fig. 4B, hemolysis percentage of red blood cells increased along with the increasing of carrier concentration over a concentration scope of 0.5–100 μg/mL. The hemolysis of MM-SN and MM–SN–NH_2-Fe can be neglected, confirming their systemic safety after administrating into the body. The cell viability of MM-SN and MM–SN–NH_2-Fe was evaluated against MCF-7 cells by MTT assay. As demonstrated in Fig. 4C, both the two carriers exhibited negligible cytotoxicity on MCF-7 cells at the concentrations of 1–50 μg/mL after 48 h culturing with samples. The results of cytotoxicity indicated that the two carries were safe to be administered.

3.3. Drug loading and release

For MM-SN, the drug loading capacity reached to 28.90%. After DOX loaded into MM–SN–NH_2-Fe, drug loading capacity was 27.76%, demonstrating that MM–SN–NH_2-Fe had good ability to incorporate drug molecules. According to the result in supporting information Table 1, DOX was loaded into the pores of carriers evidenced by the reduced specific surface area, pore volume and pore diameter. There was no significant difference in drug loading content between the two samples as illustrated in Fig. 5A. The *in vitro* release patterns were carried out under a simulated physiological condition (pH 7.4 PBS) and in acidic environments (pH 5.0 PBS) equivalent to the microenvironment in tumor to assess the feasibility to achieve pH-sensitive release. The release profiles of DOX loaded MM-SN and DOX loaded MM–SN–NH_2-Fe were presented in Fig. 5B. Almost all DOX molecules released from the two carries in the acidic medium demonstrated in Fig. 5C. The pharmacokinetics study of DOX solutions and DOX loaded carriers were determined using the HPLC-MS/MS method. The plasma drug concentration-time curves (AUC) of the compounds were shown in Fig. 6, and the original pharmacokinetic parameters were detailed in Table 2. DOX solutions performed short retention time in plasma and was eliminated promptly. On the contrast, DOX loaded carries prolonged the systemic circulation in the blood. Compared to DOX solution, DOX loaded MM-SN or MM–SN–NH_2-Fe had higher AUC and longer retention time in the systemic circulation, especially for DOX loaded MM–SN–NH_2-Fe.

3.4. Cytotoxicity assay and antitumor effect

Cytotoxic activity of DOX solution, DOX loaded MM-SN and DOX loaded MM–SN–NH_2-Fe was evaluated in MCF-7 cells and MCF-7/ADR cells by MTT assay. As shown in Fig. 7A, there was no significant difference on the basis of cytotoxicity against MCF-7 cells between DOX solution and DOX loaded carries. The comparable cytotoxicity of DOX solution and DOX loaded MM-SN might be related to the rapid drug release of DOX loaded MM-SN. In contrast, DOX loaded MM–SN–NH_2-Fe exhibited stronger cytotoxicity that can be regarded as the result of the

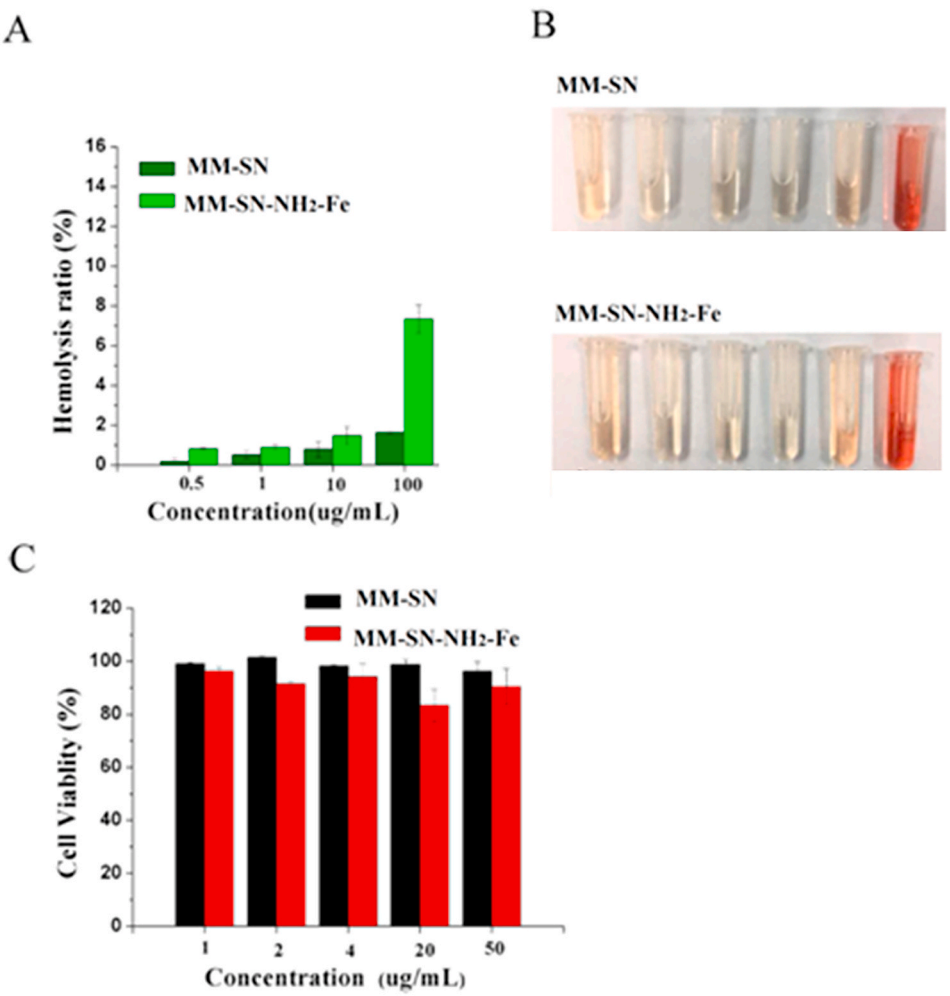

Fig. 4. Biocompatibility study of the carries. (A) Hemolysis assay, (B) hemolysis pictures of MM-SN (top) and MM–SN–NH_2-Fe (bottom), from left to right (negative, 0.5 μg/mL, 1 μg/mL, 10 μg/mL, 100 μg/mL, positive), (C) cell viability.

formation of Fe (III)-DOX complex. As displayed in Fig. 7B, for DOX solution, no obvious cytotoxicity was found against MCF-7/ADR cells at concentration of 400 ng/mL (only about 20% cells were killed). On the contrary, quite obvious cytotoxicity appeared in DOX loaded MM-SN or MM–SN–NH_2-Fe. Especially in DOX loaded MM–SN–NH_2-Fe, when the DOX equivalent concentration reached 400 ng/mL, the inhibition rate was up to 78% (larger than DOX loaded MM-SN (59%)), which was consistent with MCF-7 cytotoxicity result. The detailed half maximal inhibitory concentrations (IC_{50}) were listed in Table 1. The results demonstrated that DOX-Fe (III) complexes can cause more damage to MCF-7 cells than DOX solution because of the free radicals generating from DOX-Fe (III) [11,14,46].

The antitumor effect result was presented in Fig. 8 A and B. It showed that DOX solution, DOX loaded MM-SN and DOX loaded MM–SN–NH_2-Fe all exerted antitumor function evidenced by their abilities in inhibiting tumor growth. Furthermore, the tumor growth inhibition of DOX loaded MM–SN–NH_2-Fe was superior than DOX loaded MM-SN, confirming that MM–SN–NH_2-Fe with host-metal-guest structure facilitated antitumor function by generating more free radicals. As for the weight of mice, the normal saline group gained a little weight, DOX loaded MM-SN and DOX loaded MM–SN–NH_2-Fe reduced a little weight. DOX solution group lost most weight due to the systemic toxicity of DOX.

4. Discussion

The pore diameter of MM-SN was about 15 nm and that was enough spacious to accommodate Fe (III) and DOX, and released the loading substance quickly when it exposed to external stimuli. To our best knowledge, at this pore size (>10 nm), these were small ordered particles that have been synthesized [47]. After grafting aminopropyl then Fe (III), iron element was presented and the zeta potential of MM–SN–NH_2-Fe increased due to the cationic charges from functionalized groups on the surface.

MM–SN–NH_2-Fe entrapped DOX using solvent evaporation method into its nanopores. The drug delivery system possessed multiple drug advantages of drug delivery performances, including pH-triggered drug release, prolonged systemic circulation than DOX solution, increased cytotoxicity towards MCF-7 cells when compared with free DOX solution, and exerted more effective anti-cancer activity of DOX towards MCF-7/ADR cells compared to DOX solution and DOX loaded MM-SN. The coordination bond sensitive to low pH between DOX molecules and MM–SN–NH_2-Fe contributed to achieve pH-sensitive DOX release. In addition, the superoxide radical origin from oxidation of DOX-Fe(III) complexes contributed to stronger cytotoxicity towards MCF-7 and MCF-7/ADR cells by a series of reactions. It is believed that DOX loaded MM–SN–NH_2-Fe with high scientific value can be the promising delivery system for breast cancer treatment.

Hemolysis assay was an important evaluation of safety application for porous silica nanoparticles. For MM-SN, factors that may influence the hemolytic behavior mainly included the electrostatic interactions between silanol groups and the positively charged groups of membrane proteins, the affinity between silica and tetraalkyl ammonium groups

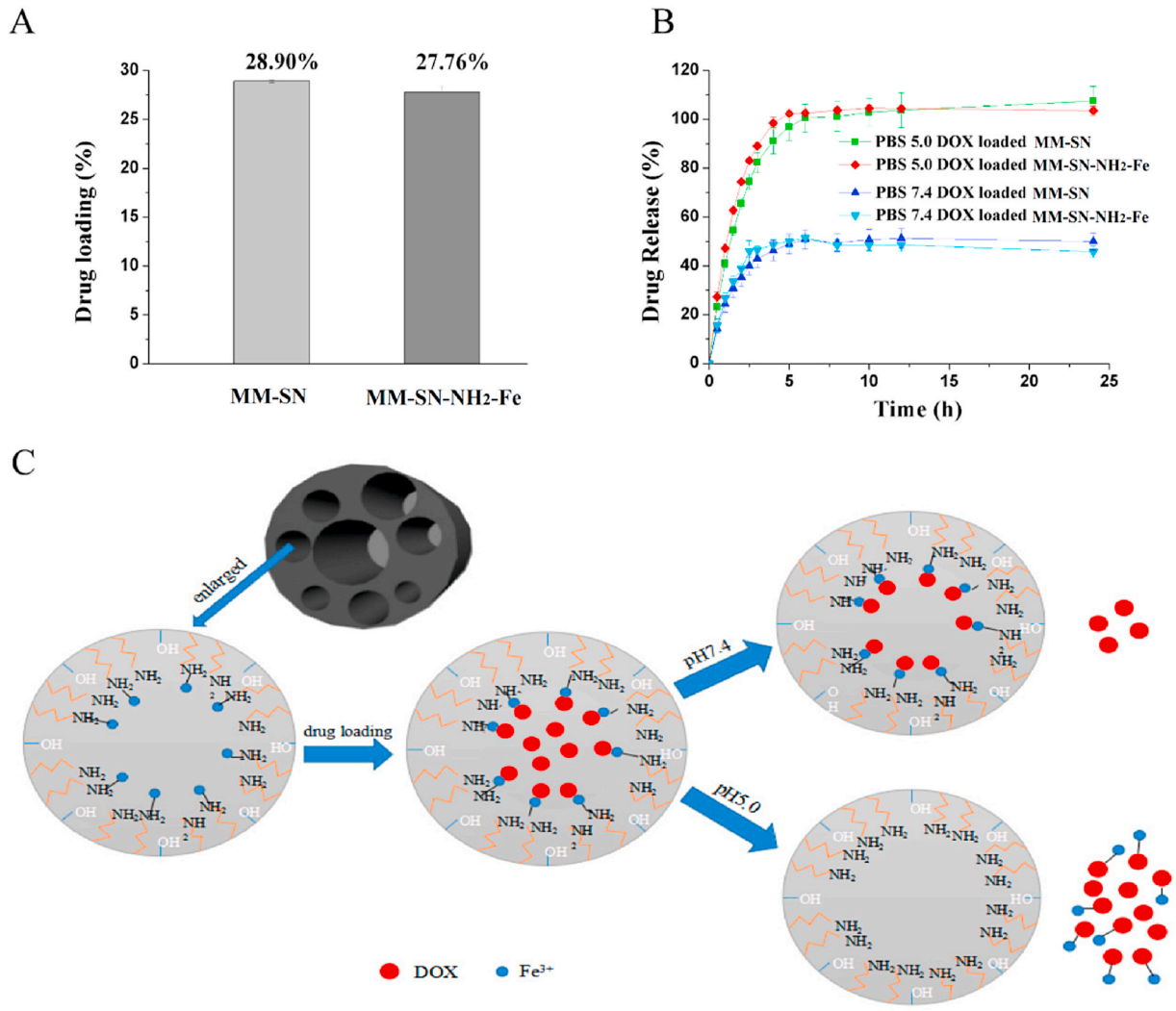

Fig. 5. (A) Drug loading, (B) release profiles and (C) illustration image of drug release.

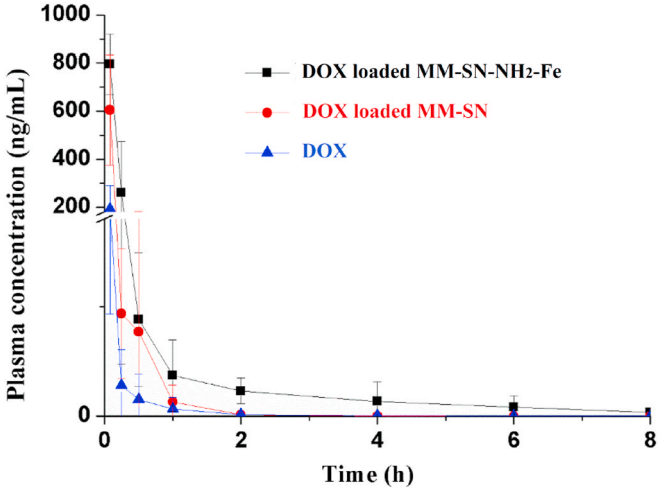

Fig. 6. Plasma concentration-time profiles of DOX solution, DOX loaded carriers after a single intravenous administration of 5 mg/kg (DOX equivalent) (n = 3).

present in the membrane of red blood cells [48],[41]. The hemolysis percentage was lower than 10%, therefore we can conclude that MM-SN and MM–SN–NH_2-Fe were safe to be administrated.

There was no significant difference in drug loading content between the two samples as illustrated in Fig. 5A. It may be related to that the

Table 1
IC_{50} of DOX solutions, DOX loaded MM-SN and DOX loaded MM–SN–NH_2-Fe against MCF-7 and MCF-7/ADR cells.

Samples	IC_{50} (ng/mL)	
	MCF-7	MCF-7/ADR
DOX solution	55.45	–
DOX loaded MM-SN	71.65	246.00
DOX loaded MM–SN–NH_2-Fe	28.31	59.79

Table 2
Pharmacokinetic parameters of DOX, DOX loaded MM-SN and DOX loaded MM–SN–NH_2-Fe.

Samples	AUC_{0-8} (μg/L*h)	Cmax (μg/L)	Tmax (h)
DOX solution	243.559 ± 363.03	192.567 ± 99.415	0.08
DOX loaded MM-SN	173.649 ± 44.341	605.5 ± 229.735	0.08
DOX loaded MM–SN–NH_2-Fe	561.744 ± 343.213	794.67 ± 126.738	0.08

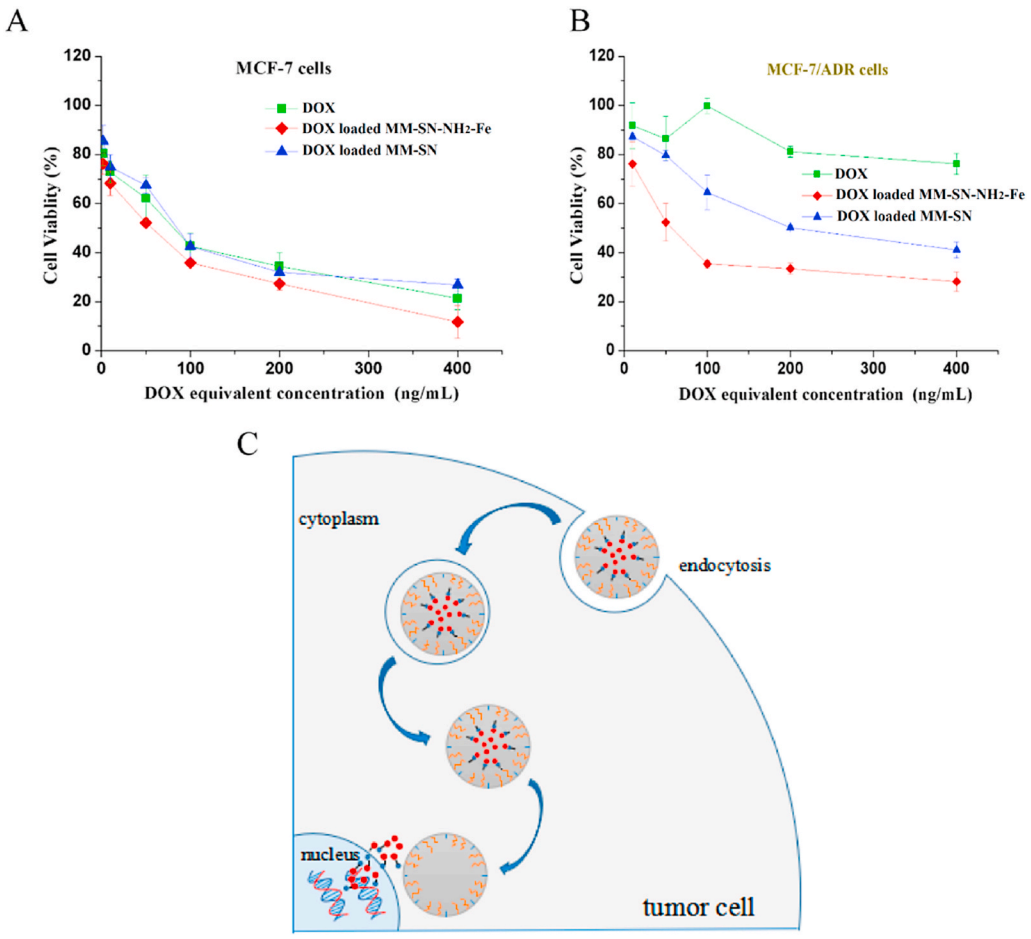

Fig. 7. Inhibition rate of (A)MCF-7 and (B) MCF-7/ADR treated with various concentrations of DOX solutions or DOX loaded carriers.

naked particles had the ability to load drug with high efficiency due to its huge pore volume that can accommodate large quantities of guest molecules. Therefore, after modification, the drug loading of the two samples was almost the same. It can be judged that both the two samples exhibited significant pH-sensitive release from the accumulative release curves. The formation of hydrogen bond between DOX molecules and MM-SN as well as the coordination bond sensitive to low pH between DOX molecules and MM–SN–NH_2-Fe contributed to achieve pH-sensitive DOX release. In vivo, DOX loaded carries prolonged the systemic circulation in the blood. Compared to DOX solution, DOX loaded MM-SN or MM–SN–NH_2-Fe had higher AUC and longer retention time in the systemic circulation, especially for DOX loaded MM–SN–NH_2-Fe, highlighting the superiority of MM–SN–NH_2-Fe in delivering DOX with high bioavailability.

DOX loaded MM–SN–NH_2-Fe performed superior cytotoxicity towards MCF-7 and MCF-7/ADR cells because the DOX-Fe(III) complexes underwent self-reduction to DOX free radical-Fe(II) complexes, which returned back to DOX-Fe(III) complexes in the presence of oxygen and formed the superoxide radical. This radical can be converted to H_2O_2 and went through the Haber–Weiss reaction catalyzed by the DOX free radical-Fe(II) complex to form the hydroxyl radical. Table 1 suggested that MCF-7/ADR cells exhibited high drug resistance to DOX, whose IC_{50} was up to 2.6×10^{21} ng/mL. In contrast, IC_{50} of DOX loaded MM–SN–NH_2 or MM–SN–NH_2-Fe was 246 ng/mL and 59.79 ng/mL respectively. It could be judged that the carries could increase cytotoxicity of DOX to MCF-7/ADR as illustrated in Fig. 7C and thus lead to more effective anti-cancer activity of DOX to MCF-7/ADR cells [49,50]. The MDR reversion effect of MM–SN–NH_2-Fe was another outstanding performance in delivering DOX. The host-metal-guest structure of MM–SN–NH_2-Fe with superior performances in delivering DOX has great value in anticancer treatment. The tumor growth inhibition of DOX loaded MM–SN–NH_2-Fe was superior than DOX loaded MM-SN, confirming that MM–SN–NH_2-Fe with host-metal-guest structure facilitated antitumor function by generating more free radicals. Therefore, DOX loaded MM–SN–NH_2-Fe with best antitumor effect and systemic safety can be rendered as an outstanding DOX delivery system.

5. Conclusions

Fe(III) loaded porous silica nanoparticles was established by preparing host-metal-guest carrier named as MM–SN–NH_2-Fe. The release performance of DOX loaded MM–SN–NH_2-Fe showed higher pH response release by cleavage of the Fe-DOX bond or the NH_2–Fe coordination bond. Cytotoxicity result demonstrated that DOX loaded MM–SN–NH_2-Fe presented stronger anti-cancer activity against MCF-7 and MCF-7/ADR cells compared to that of free DOX and DOX loaded MM-SN. In vivo, DOX based nanoparticles significantly prolonged systemic circulation and DOX loaded MM–SN–NH_2-Fe exerted the best antitumor effect. DOX loaded MM–SN–NH_2-Fe with pH-triggered release and superior anti-cancer activity for DOX delivery system has great value in anticancer treatment.

CRediT authorship contribution statement

Ruoshi Zhang: Formal analysis, Writing - review & editing. **Xin Wang:** Investigation. **Na Fan:** Data curation. **Jing Li:** Project administration, Writing - original draft.

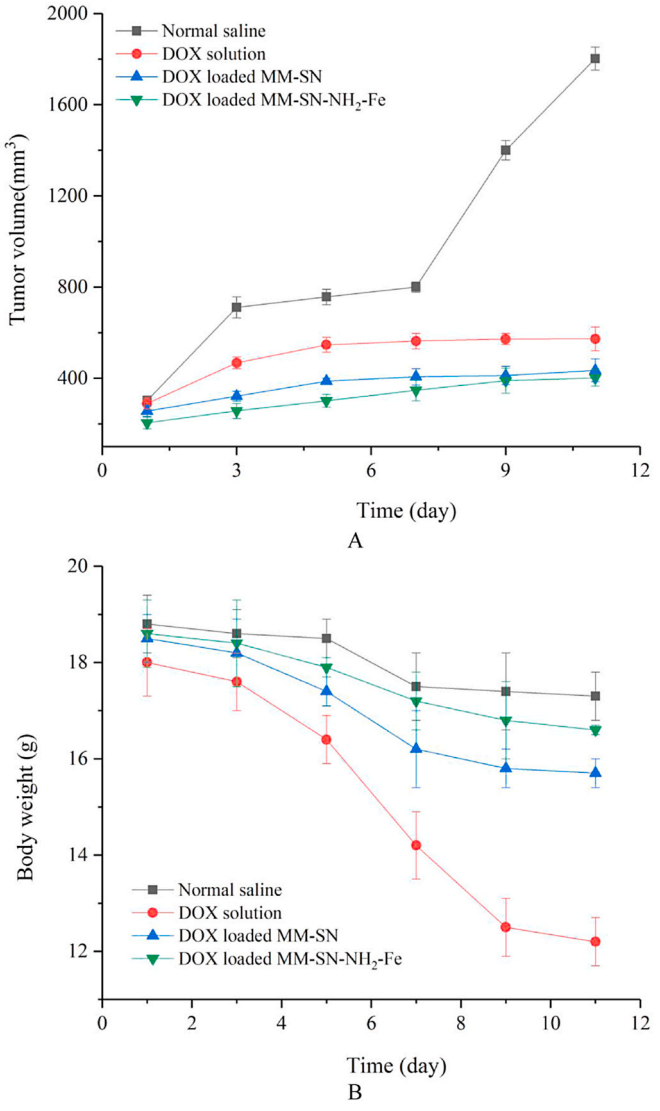

Fig. 8. (A) The anticancer efficacy of samples was evaluated in 4T1-bearing Balb/C mice.(B) The change of body weight of samples during administration.

Declaration of competing interest

The authors declare that they have no known competing financial interests or personal relationships that could have appeared to influence the work reported in this paper.

Appendix A. Supplementary data

Supplementary data to this article can be found online at https://doi.org/10.1016/j.micromeso.2020.110589.

References

[1] E.B.C.T.C. Group, J. Godwin, Tamoxifen for early breast cancer: an overview of the randomised trials, Lancet 351 (1998) 1451–1467.
[2] G. Bianchini, J.M. Balko, I.A. Mayer, M.E. Sanders, L. Gianni, Triple-negative breast cancer: challenges and opportunities of a heterogeneous disease, Nat. Rev. Clin. Oncol. 13 (2016) 674–690.
[3] J. Shen, Q. He, Y. Gao, J. Shi, Y. Li, Mesoporous silica nanoparticles loading doxorubicin reverse multidrug resistance: performance and mechanism, Nanoscale 3 (2011) 4314–4322.
[4] J. Li, X. Du, N. Zheng, L. Xu, J. Xu, S. Li, Contribution of carboxyl modified chiral mesoporous silica nanoparticles in delivering doxorubicin hydrochloride in vitro: pH-response controlled release, enhanced drug cellular uptake and cytotoxicity, Colloids Surf. B Biointerfaces 141 (2016) 374–381.
[5] J. O'Shaughnessy, Liposomal anthracyclines for breast cancer: overview, Oncol. 8 (Suppl 2) (2003) 1–2.
[6] D.A. Gewirtz, A critical evaluation of the mechanisms of action proposed for the antitumor effects of the anthracycline antibiotics adriamycin and daunorubicin, Biochem. Pharmacol. 57 (1999) 727–741.
[7] R. Petrioli, A.I. Fiaschi, E. Francini, A. Pascucci, G. Francini, The role of doxorubicin and epirubicin in the treatment of patients with metastatic hormone-refractory prostate cancer, Canc. Treat Rev. 34 (2008) 710–718.
[8] W. Xin, L. Chang, F. Na, L. Jing, Z. He, S. Jin, Multimodal nanoporous silica nanoparticles functionalized with aminopropyl groups for improving loading and controlled release of doxorubicin hydrochloride, Mater. Sci. Eng. C 78 (2017) 370–375.
[9] P.M. May, G.K. Williams, D.R. Williams, Solution chemistry studies of adriamycin–iron complexes present in vivo, Eur. J. Canc. 16 (1980) 1275–1276.
[10] E.L. Kostoryz, D.M. Yourtee, Oxidative mutagenesis of doxorubicin-Fe(III) complex, Mutat. Res. Genet. Toxicol. Environ. Mutagen 490 (2001) 131–139.
[11] H. Beraldo, A. Garniersuillerot, L. Tosi, F. Lavelle, Iron(III)-adriamycin and iron (III)-daunorubicin complexes: physicochemical characteristics, interaction with DNA, and antitumor activity, Biochemistry 24 (1985) 284–289.
[12] J.R. Muindi, B.K. Sinha, L. Gianni, C.E. Myers, Hydroxyl radical production and DNA damage induced by anthracycline-iron complex, FEBS Lett. 172 (1984) 226–230.
[13] L. Gianni, J.L. Zweier, A. Levy, C.E. Myers, Characterization of the cycle of iron-mediated electron transfer from Adriamycin to molecular oxygen, J. Biol. Chem. 260 (1985) 6820–6826.
[14] C. Myers, L. Gianni, J. Zweier, J. Muindi, B.K. Sinha, H. Eliot, Role of iron in adriamycin biochemistry, Fed. Proc. 45 (1986) 2792–2797.
[15] Y. Wang, Q. Zhao, Y. Hu, L. Sun, L. Bai, T. Jiang, S. Wang, Ordered nanoporous silica as carriers for improved delivery of water insoluble drugs: a comparative study between three dimensional and two dimensional macroporous silica, Int. J. Nanomed. 8 (2013) 4015–4031.
[16] Y. Zhang, J. Wang, X. Bai, T. Jiang, Q. Zhang, S. Wang, Mesoporous silica nanoparticles for increasing the oral bioavailability and permeation of poorly water soluble drugs, Mol. Pharm. 9 (2012) 505–513.
[17] S.H. Wu, Y. Hung, C.Y. Mou, Mesoporous silica nanoparticles as nanocarriers, Chem. Commun. 47 (2011) 9972–9985.
[18] C.P. Tsai, C.Y. Chen, Y. Hung, F.H. Chang, C.Y. Mou, Monoclonal antibody-functionalized mesoporous silica nanoparticles (Msn) for selective targeting breast cancer cells, J. Mater. Chem. 19 (2009) 5737–5743.
[19] S.G. Wainwright, C.M.A. Parlett, R.A. Blackley, W. Zhou, A.F. Lee, K. Wilson, D. W. Bruce, True liquid crystal templating of SBA-15 with reduced microporosity, Microporous Mesoporous Mater. 172 (2013) 112–117.
[20] L. Minati, V. Antonini, M.D. Serra, G. Speranza, F. Enrichi, P. Riello, pH-activated doxorubicin release from polyelectrolyte complex layer coated mesoporous silica nanoparticles, Microporous Mesoporous Mater. 180 (2013) 86–91.
[21] H. Zheng, S. Che, Amino/quaternary ammonium groups bifunctionalized large pore mesoporous silica for pH-responsive large drug delivery, RSC Adv. 2 (2012) 4421–4429.
[22] J. Li, L. Xu, B. Yang, H. Wang, Z. Bao, W. Pan, S. Li, Facile synthesis of functionalized ionic surfactant templated mesoporous silica for incorporation of poorly water-soluble drug, Int. J. Pharm. 492 (2015) 191–198.
[23] J. Li, L. Xu, H. Liu, Y. Wang, Q. Wang, H. Chen, W. Pan, S. Li, Biomimetic synthesized nanoporous silica@poly(ethyleneimine)s xerogel as drug carrier: characteristics and controlled release effect, Int. J. Pharm. 467 (2014) 9–18.
[24] J. Li, Y. Guo, H. Li, L. Shang, S. Li, Superiority of amino-modified chiral mesoporous silica nanoparticles in delivering indometacin, Artificial Cells Nanomed. Biotechnol. 46 (2018) 1085–1094.
[25] N. Zheng, J. Li, C. Xu, L. Xu, S. Li, L. Xu, Mesoporous silica nanorods for improved oral drug absorption, Artificial Cells Nanomed. Biotechnol. 46 (2018) 1132–1140.
[26] M.S. Kim, Soluplus-coated colloidal silica nanomatrix system for enhanced supersaturation and oral absorption of poorly water-soluble drugs, Artificial Cells Nanomed. Biotechnol. 41 (2013) 363–367.
[27] S. Giri, B.G. Trewyn, M.P. Stellmaker, V.S. Lin, Stimuli-responsive controlled-release delivery system based on mesoporous silica nanorods capped with magnetic nanoparticles, Angew. Chem. 44 (2005) 5038–5044.
[28] J. Wang, H. Liu, F. Leng, L. Zheng, J. Yang, W. Wang, C.Z. Huang, Autofluorescent and pH-responsive mesoporous silica for cancer-targeted and controlled drug release, Microporous Mesoporous Mater. 186 (2014) 187–193.
[29] D. He, X. He, K. Wang, M. Chen, J. Cao, Y. Zhao, Reversible stimuli-responsive controlled release using mesoporous silica nanoparticles functionalized with a smart DNA molecule-gated switch, J. Mater. Chem. 22 (2012) 14715–14721.
[30] J. Yao, J. Feng, J. Chen, External-stimuli responsive systems for cancer theranostic, Asian J. Pharm. Sci. 11 (2016) 585–595.
[31] F. Qu, G. Zhu, S. Huang, S. Li, J. Sun, D. Zhang, S. Qiu, Controlled release of Captopril by regulating the pore size and morphology of ordered mesoporous silica, Microporous Mesoporous Mater. 92 (2006) 1–9.
[32] S. Angelos, Y.W. Yang, N.M. Khashab, J.F. Stoddart, J.I. Zink, Dual-controlled nanoparticles exhibiting AND logic, J. Am. Chem. Soc. 131 (2009) 11344–11346.
[33] C.R. Steven, G.A. Busby, C. Mather, B. Tariq, M.L. Briuglia, D.A. Lamprou, A. J. Urquhart, M.H. Grant, S.V. Patwardhan, Bioinspired silica as drug delivery systems and their biocompatibility, J. Mater. Chem. B 2 (2014) 5028–5042.
[34] B. Wang, D. Yang, J.Z. Zhang, C. Xi, J. Hu, Stimuli-responsive polymer covalent functionalization of graphene oxide by Ce(IV)-Induced redox polymerization, J. Phys. Chem. C 115 (2011) 24636–24641.
[35] T. Jin, D. Wu, X. Liu, J. Xu, B. Ma, Y. Ji, Y. Jin, S. Wu, T. Wu, K. Ma, Intra-articular delivery of celastrol by hollow mesoporous silica nanoparticles for pH-sensitive

anti-inflammatory therapy against knee osteoarthritis, J. Nanobiotechnol. 18 (2020) 94.
[36] K. Sun, Z. Gao, Y. Zhang, H. Wu, C. You, S. Wang, P. An, C. Sun, B. Sun, Enhanced highly toxic reactive oxygen species levels from iron oxide core-shell mesoporous silica nanocarrier-mediated Fenton reactions for cancer therapy, J. Mater. Chem. B 6 (2018) 5876–5887.
[37] Y. Berro, S. Gueddida, Y. Bouizi, C. Bellouard, E. Bendeif, A. Gansmuller, A. Celzard, V. Fierro, D. Ihiawakrim, O. Ersen, M. Kassir, F. El Haj Hassan, S. Lebegue, M. Badawi, N. Canilho, A. Pasc, Imprinting isolated single iron atoms onto mesoporous silica by templating with metallosurfactants, J. Colloid Interface Sci. 573 (2020) 193–203.
[38] L. Wang, M. Huo, Y. Chen, J. Shi, Iron-engineered mesoporous silica nanocatalyst with biodegradable and catalytic framework for tumor-specific therapy, Biomaterials 163 (2018) 1–13.
[39] A. Roucher, M. Emo, F. Vibert, M. Stébé, V. Schmitt, F. Jonas, R. Backov, J. Blin, Investigation of mixed ionic/nonionic building blocks for the dual templating of macro-mesoporous silica, J. Colloid Interface Sci. 533 (2019) 385–400.
[40] J. Lee, M. Kim, T. Nguyen, J. Kim, Hollow mesoporous silica nanoparticles with extra-large mesopores for enhanced cancer vaccine, ACS Appl. Mater. Interfaces 12 (2020) 34658–34666.
[41] X. Wang, C. Li, N. Fan, J. Li, Z. He, J. Sun, Multimodal nanoporous silica nanoparticles functionalized with aminopropyl groups for improving loading and controlled release of doxorubicin hydrochloride, Materials science & engineering, C, Mater. Biol. Appl. 78 (2017) 370–375.
[42] L. Jing, X. Lu, Z. Nan, W. Hongyu, L. Fangzheng, L. Sanming, Biomimetic synthesized bimodal nanoporous silica: bimodal mesostructure formation and application for ibuprofen delivery, Mater. Sci. Eng. C Mater. Biol. Appl. 58 (2016) 1105–1111.
[43] J. Goscianska, A. Olejnik, I. Nowak, M. Marciniak, R. Pietrzak, Ordered mesoporous silica modified with lanthanum for ibuprofen loading and release behaviour, Eur. J. Pharmaceutics & Biopharm. Offic.J. Arbeitsgemeinschaft Fu?r Pharmazeutische Verfahrenstechnik E V 94 (2015) 550–558.
[44] Y. Zhang, Z. Zhi, T. Jiang, J. Zhang, Z. Wang, S. Wang, Spherical mesoporous silica nanoparticles for loading and release of the poorly water-soluble drug telmisartan, J. Control. Release Offic. J. Control. Release Soc. 145 (2010) 257–263.
[45] Y. Wang, N. Han, Q. Zhao, L. Bai, J. Li, T. Jiang, S. Wang, Redox-responsive mesoporous silica as carriers for controlled drug delivery: a comparative study based on silica and PEG gatekeepers, Eur. J. Pharmaceut. Sci. 72 (2015) 12–20.
[46] J.L. Zweier, Iron-mediated formation of an oxidized adriamycin free radical, Biochim. Biophys. Acta 839 (1985) 209–213.
[47] J. Sun, H. Zhang, R. Tian, D. Ma, X. Bao, D.S. Su, H. Zou, Ultrafast enzyme immobilization over large-pore nanoscale mesoporous silica particles, Chem. Commun. 12 (2006) 1322–1324.
[48] J. Depasse, J. Warlus, Relation between the toxicity of silica and its affinity for tetraalkylammonium groups. Comparison between Si0 2 and Ti0 2, J. Colloid Interface Sci. 56 (1976) 618–621.
[49] Q. He, J. Shi, MSN anti-cancer nanomedicines: chemotherapy enhancement, overcoming of drug resistance, and Metastasis inhibition, Adv. Mater. 26 (2014) 391–411.
[50] Q. He, Z. Zhang, Y. Gao, J. Shi, Y. Li, Intracellular localization and cytotoxicity of spherical mesoporous silica Nano- and Microparticles, Small 5 (2009) 2722–2729.